IEEE Access
Multidisciplinary | Rapid Review | Open Access Journal

Received September 15, 2020, accepted October 9, 2020, date of publication October 13, 2020, date of current version October 30, 2020.

Digital Object Identifier 10.1109/ACCESS.2020.3030617

Benchmarking a Commercial (Sub-)THz Focal Plane Array Against a Custom-Built Millimeter-Wave Single-Pixel Camera

SANG-HEE SHIN, (Graduate Student Member, IEEE), AND STEPAN LUCYSZYN, (Fellow, IEEE)
Department of Electrical and Electronic Engineering, Imperial College London, London SW7 2AZ, U.K.

Corresponding author: Stepan Lucyszyn (s.lucyszyn@imperial.ac.uk)

This work was supported in part by the U.K. Space Agency's Centre for Earth Observation Instrumentation (CEOI) under Grant RP10G0435A202, and in part by the U.K. Space Agency under Grant NSTP3-FT-046.

ABSTRACT For the first time, the characteristics of an evolving commercial camera technology that can operate at millimeter-wave frequencies has been independently investigated. In this work, we benchmark the TeraSense camera against a custom-built single-pixel camera at W-band, for image quality and aperture reflectance. It is found that the Tera-1024 TeraSense camera exhibits limited image resolution and fidelity, with significant levels of systematic spatial noise. In a poor signal-to-noise ratio scenario, the addition of random noise exacerbates these problems. Possible causes of both beam and image distortion have been identified in quasi-optical applications, which gives important insight into the best use of (sub-)THz cameras and interpretation of their images. Inherent standing waves caused by the significant power reflectance of the camera aperture is investigated in detail. A simple W-band one-port quasi-optical scalar network analyzer is developed, to determine the levels of reflectance for both cameras, with its bespoke calibration routine derived from first principles – providing a low-cost solution for many non-destructive testing applications. It is found that the TeraSense camera (with additional RAM) and single-pixel camera (having default RAM) have measured reflectance values of 27% and 3%, respectively, over a corresponding aperture area ratio of approximately 714:1. While our single-pixel camera provides excellent image resolution and fidelity, it inherently suffers from very slow raster-scanning speeds and operational bandwidth limitations. For this reason, the TeraSense camera technology is excellent for performing qualitative measurements in real time, with the caveats outlined in this paper.

INDEX TERMS Millimeter-wave, W-band, sub-THz, terahertz, focal plane array, camera, quasi-optics.

I. INTRODUCTION

Radiometric imaging technologies are based on measuring thermal noise, either naturally emitted by a body (using a 'passive radiometer') or enhanced by illumination of the body using external sources, whereby the coherent signal energy is absorbed by the body and re-radiated as additional incoherent thermal noise energy (using an 'active radiometer'). Radiometry in the thermal infrared (IR) spectrum (for example at frequencies from 20 THz up to 40 THz, corresponding to wavelengths in free-space from 14 μm down to 7 μm) has the advantage of relatively good image resolution and fidelity with commercially available cameras, but has limitations on penetration depth.

The associate editor coordinating the review of this manuscript and approving it for publication was Pu-Kun Liu.

The sub-THz band (i.e., any frequencies below 1 THz) offers the advantage of unprecedented penetration depth, for seeing through materials such as fabric, ceramic, plastic, leather and paper/cardboard. Although, above *ca.* 600 GHz, electromagnetic scattering off woven fabrics is still a major limitation. In addition, as a general rule of thumb, the cost of implementing technologies increase with increasing frequency, up into the infrared spectrum. For this reason, moving down the frequency spectrum gives improved penetration depth and can potentially be cheaper, but with low spatial resolution from a compact camera. The millimeter-wave spectrum (30 GHz up to 300 GHz, corresponding to wavelengths in free-space from 10 mm down to 1 mm) offers a compromise in terms of penetration depth against spatial resolution; technologies at these frequencies will be the focus of this paper.

Operating at millimeter frequencies has a number of other important issues for their practical implementation. The first is that Planck's law shows that the thermal 'brightness' of a body diminishes as frequency decreases; having its peak value within the IR spectrum for a body at room temperature. In contrast, atmospheric attenuation tends to improve as frequency decreases; although there are spectral peaks that should be avoided, due molecular resonances (oxygen and water absorption bands) – this explains why millimeter-wave systems operate below *ca.* 40 GHz and between 70 GHz and 100 GHz (avoiding the broad and strong oxygen absorption band, centered at approximately 60 GHz) [1].

There are a number of room-temperature radiometric imaging systems available on the open market, used mainly for industrial non-destructive testing and security screening applications – based on the following generic technologies: (i) very high performance, extremely high cost heterodyne radiometers; (ii) medium performance, very high cost pre-amplified direct detection radiometers; and (iii) low performance, medium cost non-pre-amplified direct detection radiometers, which requires additional critically placed 'active' source(s) of illumination. An example of (iii) is the US-Russian TeraSense camera; the technical details of which are inferred from their recent publications [2]–[4]. Their mid-range Tera-1024 (sub-)THz camera has a 2-D focal plane array (FPA) with 32 × 32 pixels. Each pixel has a plasmonic detector, made from a patented GaAs/AlGaAs heterostructure technology [2]. The embedded two-dimensional electron system (2DES) channel (having a resistance of 100 Ω [3]) is grown on a semi-insulating GaAs substrate. Two inner gates (with ∼0.5 V of asymmetric DC bias) create a photon microcavity, having a width and length of 15 μm and 20 μm, respectively. These input electrodes are fed by a broadband on-chip log-periodic antenna, having an external diameter of 1.5 mm [3]. With a 1.5 mm pitch between pixels, the half-wavelength spacing provides optimal performance at 100 GHz. The microcavity light modes couple with the 2DES plasma modes, having a sub-half-micron vertical separation distance, to excite confined relativistic plasmons (damped plasma waves) that can propagate along the 2DES channel at room temperature [2]–[4]. The rectified output photo-response signal is taken from two outer (source and drain) electrodes. The amplitude of this signal provides information about the power intensity of the incident electromagnetic radiation (recorded in arbitrary units).

According to Nyquist, the theoretical minimum spatial resolution of the camera is half the wavelength of the electromagnetic radiation being observed. The TeraSense camera has a certified spectral range from 50 GHz up to 700 GHz [5]. Moreover, at a room temperature of approximately 296 K (23°C), the detector has a post-amplification voltage responsivity of 50 kV/W and noise equivalent power (NEP) of 1 nW/$\sqrt{\text{Hz}}$ [3] from 10 GHz to 1 THz.

When compared to uncooled microbolometer (ultra-broadband thermal detector) based FPA cameras optimized for THz applications, which can require a post-detection integration time of tens of milliseconds, plasmonic detectors have a few order of magnitude shorter response times with its room temperature NEP being an order of magnitude higher, an external 'active' illumination source is required with both uncooled microbolometer and TeraSense cameras.

Nevertheless, with the TeraSense camera being able to operate at millimeter-wave frequencies, this state-of-the-art technology represents a unique and valuable room-temperature imaging tool for the scientific and engineering communities; for example, in the absence of an expensive professional antenna test range [6]. With this in mind, it is important to independently investigate the performance of this camera within a quasi-optical environment.

II. MILLIMETER-WAVE CAMERAS

Cameras provide quick and easy ways of measuring quasi-optical features of beams, such as cross-sectional images and intensity distributions along the propagation z-axis.

For example, at (sub-)THz frequencies, there are at least two uncooled microbolometer FPA cameras on the market; both being relatively expensive. The TZCam (from i2S, France) has a 320 × 240 pixel array with a 50 μm pitch that provides an associated peak performance at ∼3 THz, with a specified frequency of operation from 300 GHz to 5 THz; requiring an additional electronically-controlled mechanical shutter for zero baseline level calibration (with repeated calibration-measurement cycles needed to increase the signal-to-noise ratio) [7]. Also, the MICROXCAM-384i-THz (from INO, Canada) has a 384 × 288 pixel array with a 35 μm pitch that provides an associated peak performance at ∼4 THz, with a specified frequency of operation from 94 GHz to 4.25 THz [8]. However, the next-generation of (non-pre-amplified direct detection) CMOS FPA cameras are aimed at the low-cost market. For example, the TicMOS-1kpx (from TicWave, Germany) has a 32 × 32 pixel array and a -3 dB bandwidth between 0.75 THz to 1 THz, with a specified frequency of operation from 100 GHz to 4 THz [9]. More information on these products is available [10], [11].

Here, we benchmark the medium-cost Tera-1024 camera against a custom-built single-pixel camera at W-band (75 GHz to 110 GHz), for image quality and aperture reflectance.

A. SINGLE-PIXEL RASTER SCANNED

A single-pixel raster-scanning camera is custom built, based on one millimeter-wave diode detector, 3-D scanning mechanism and an automated data acquisition module. 3-D printed brackets and mounts are employed, with an optical breadboard for precision alignment. A block diagram, illustrating each component of the single-pixel camera, is shown on Fig. 1(a).

The camera has a square-law detector (Millitech DXP-10 Schottky barrier beam lead diode detector [12]), operating across W-band, with a standard open-ended WR-10 waveguide aperture (2.54 mm × 1.27 mm) surrounded by radiation absorbent material (RAM).

For creating 2-D cross-sectional images, perpendicular to the propagation z-axis, the detector raster scans over the horizontal and vertical x-y plane. Figure 1(b) shows a simplified illustration for our raster scanning sequence.

The 3-axes (x, y and z) scanning mechanism is actuated using three pairs of stepper motors and 8 mm lead screws. Each axis is guided with a pair of linear-rails and matching roller bearings. The stepper motors are controlled with two microcontrollers (ATmega328P and ATmega2560) [13], [14]. Depending on the spatial resolution setting, the microcontrollers sets the direction, speed and step-counts for the stepper motors. The stepper motors are synchronized to accommodate the sampling rates for the data acquisition module. The minimum achievable pixel size (d_{px},d_{py}) with our setup is ~10 μm.

The basic data acquisition module employs a lock-in amplifier and two 16-bit (Texas Instrument ADS1115 [15]) analog-to-digital converters (ADCs), which feed the microcontroller boards that are synchronized with the scanning mechanism. As an optional improvement, employing an additional first-order anti-aliasing low-pass filter (between the detector and ADC), the noise floor would be significantly reduced; enhancing the temporal resolution for the single pixel camera.

B. TERASENSE FPA

With any FPA, image quality is dependent on both spatial resolution and pixel fidelity. The latter is a function of the number and distribution of pixels that are faulty and those with large deviations in responsivity. The TeraSense camera has a a specified permissible number of faulty pixels of up to 3% and specified pixel-to-pixel responsivity deviation from the mean value is within 20%; requiring additional image calibration/correction measures. As with the single-pixel camera, external active illumination is needed [3].

Since the TeraSense camera has limited spatial resolution, faulty pixels can corrupt beam profile images. In addition, faulty pixels near the center of a beam makes it difficult to identify the location of peak intensity. Also, over a period of months, the number of faulty pixels increased. To expose and map the faulty pixels, the camera's aperture is fully illuminated by a beam at maximum exposure and 100 frames are accumulated. Initially, 24 faulty pixels were recorded, with 16 more faulty pixels identified after 30 months. The quasi-optical measurements for this work are undertaken with between 26 and 40 faulty pixels. Figure 2 shows the mapped locations of faulty pixels. Clearly, as the number of both dead and malfunctioning pixels increase, the need for sophisticated image processing increases and image fidelity becomes more problematic.

A performance summary for each camera is given in Table 1.

C. BEAM SOURCES

For this study, two Gunn diode modules are used (Millitech GDM-12-WB-17M, operating at 76 GHz and Millitech GDM-10-0-17H, operating at 92 GHz [12]). In both cases, an isolator (Millitech JFL-10-NI [12]) is employed to protect the Gunn diode modules from impedance mismatch reflections. With the 76 GHz source, an additional WR-12 to WR-10 waveguide transition is inserted between the Gunn diode module and isolator. For biasing the sources, a separate Gunn Modulator Regulator (Millitech GMR) is employed.

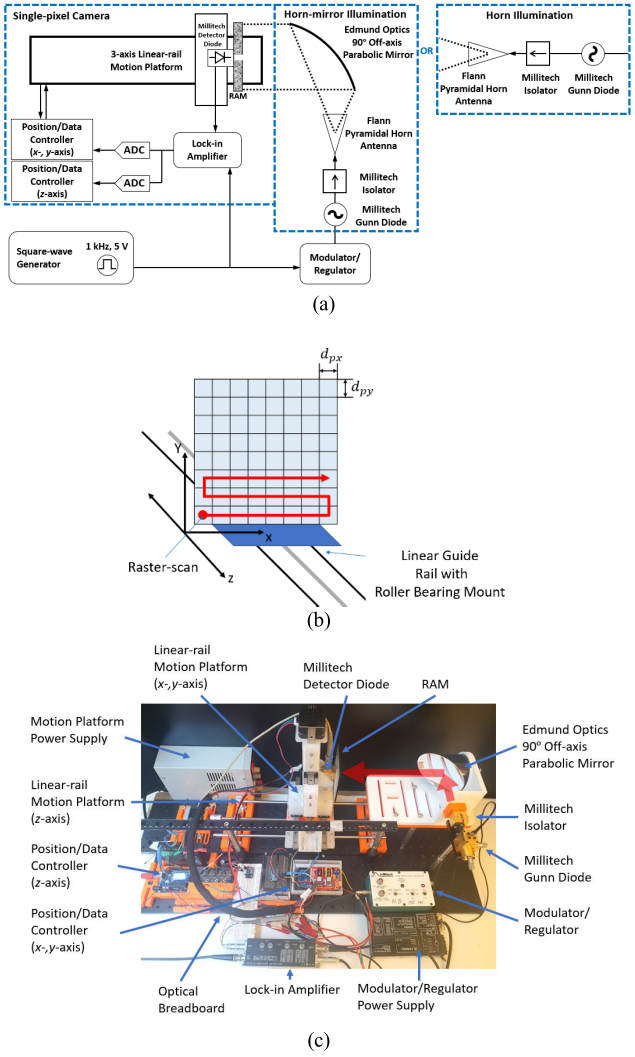

FIGURE 1. Custom-built single-pixel raster-scanning camera: (a) basic block diagram; (b) illustration of raster-scanning sequence; and (c) complete single-pixel camera system.

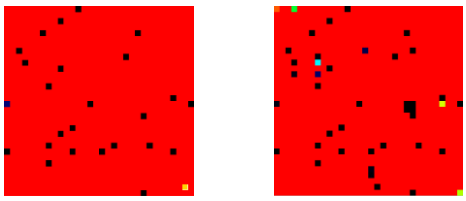

FIGURE 2. Faulty pixel map for our Tera-1024 camera with a count of: (a) 26, prior to this work; (b) 40, after this work. Black squares represent dead pixels (no output) and blue/green/yellow pixels give a false reading.

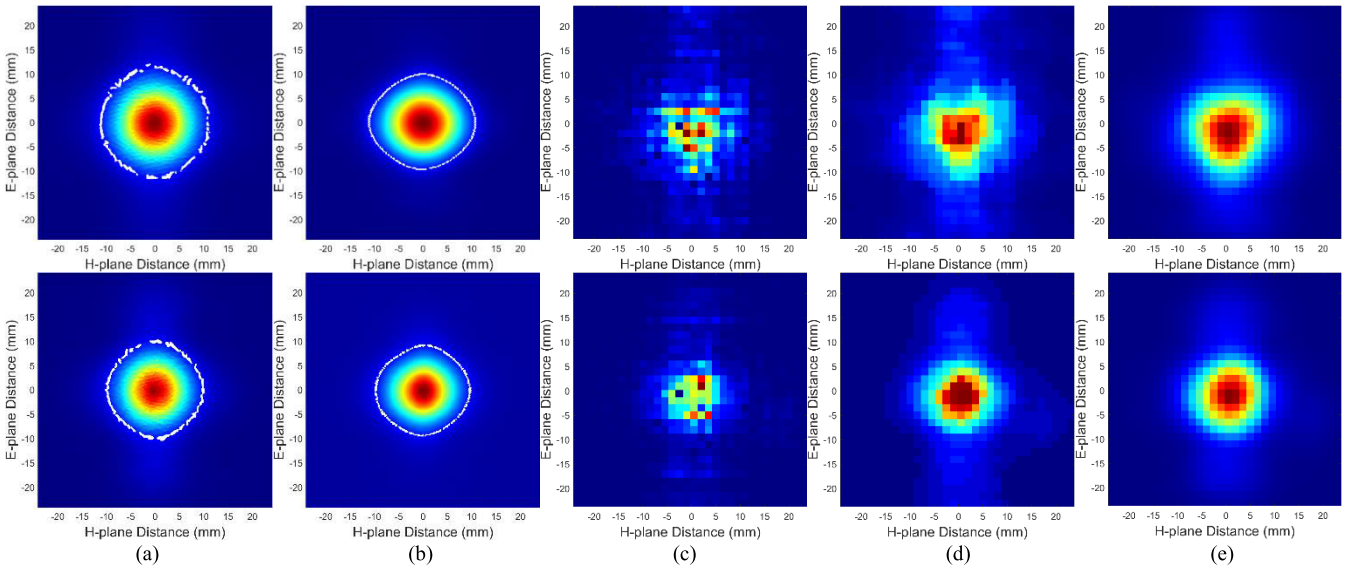

FIGURE 3. EM Simulated and measured diverging beam cross section images (normalized values) at 76 GHz (above) and 92 GHz (below) with a 30 mm separation distance between antenna and camera apertures: (a) Reference HFSS simulation (raw); (b) single-pixel camera (raw); (c) TeraSense camera (raw); (d) TeraSense camera (proprietary median-smooth filter); and (e) TeraSense camera (MATLAB 'disk smooth' filter). The white loci in 3(a)-3(b) represent the extracted $1/e^2$ boundaries.

TABLE 1. Performance summary for the single-pixel and TeraSense cameras.

Specifications	Camera	
	Single-pixel	TeraSense
Step/Pixel Size (mm)	0.2 (step)	1.5 (pixel)
Pixel Density (pixels/cm^2)	2500	44
Faulty Pixels	0	26
Pixel Responsibility Deviation (%)	≈ 0	≤ 20
Exposure Time	3 – 6 hrs	< 1 min
Relative Cost	low	medium

When square-wave modulation is needed, an external modulator (1 kHz, 5 V) is used to clock the GMR.

As shown in Fig. 1(a), with a typical quasi-optical (QO) set-up, a pyramidal horn antenna (FLANN 27240-20 [16]) is employed with the Gunn diode module to radiate a diverging beam. When a collimated beam is needed, a 90^o off-axis parabolic mirror (Edmund Optics 35-522 [17]) is placed 76.2 mm away from the pyramidal horn antenna's effective focal point. It is worth noting that a perfect collimation is unachievable with a pyramidal horn antenna, because it does not represent an ideal point source.

III. MEASURING IMAGE QUALITY

Camera image performance is investigated with two beams. First, at a fixed distance, the horn antenna directly illuminates the camera, with its diverging beam within the radiating near field of the antenna. Second, the horn antenna feeds the 90° off-axis parabolic mirror to illuminate the camera with a near-collimated beam. With the latter, both cameras are set to acquire 2-D cross-sectional images of the beam at different distances along the propagation z-axis. Here, the single-pixel camera is chosen to acquire images with a modest resolution step size setting of $d_{px} = d_{py} = 200\ \mu$m.

A. DIVERGING BEAM

With the diverging beam, the distance between the antenna and camera apertures is fixed at 30 mm. Raw (unfiltered in this context) 2-D images showing the spatial beam profiles from electromagnetic (EM) simulation software (HFSS) and measured by the cameras, at 76 GHz and 92 GHz, are shown on Fig. 3(a) to 3(c). In addition, images created using TeraSense's proprietary median-smooth filter is applied (at the maximum level), shown in Fig. 3(d). Also, MATLAB's 'disk smooth' filter [18] is applied to the raw images from the TeraSense camera and the results are shown in Fig. 3(e).

From Fig. 3, the rough shape and size of the incident beam can be estimated by visual inspection of the raw images from both cameras. However, with the TeraSense camera, the poor image resolution and fidelity prohibit extraction of useful information (e.g., cross-sectional beam profiles and beam widths). In contrast, with the single-pixel camera, the raw image can accurately identify the $1/e^2$ boundaries and beam centers. With smooth filters, the camera images resemble those simulated. Figure 3(d) and 3(e), clearly shows significant improvements on image quality for the beam shapes.

For example, beam cross section profiles are plotted for the magnetic(H)- and electric(E)-field planes at 76 GHz and 92 GHz and the results are shown in Fig. 4. Here, the full width at half maximum (FWHM) and $1/e^2$ beam widths are extracted and given in Table 2. It can be seen that the raw image from this single-pixel camera is in excellent agreement

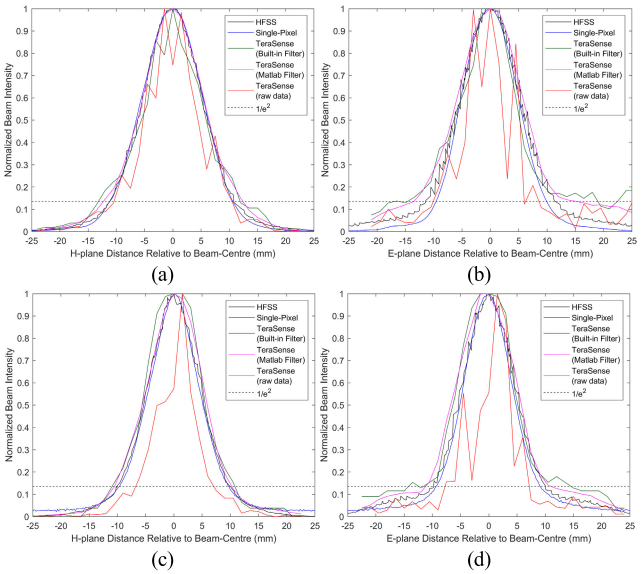

FIGURE 4. Orthogonal beam cross-sectional profiles from reference HFSS simulations (raw), single-pixel (raw) and TeraSense camera images with 30 mm separation distance between the antenna and camera apertures: (a) H-field plane at 76 GHz; (b) E-field plane at 76 GHz; (c) H-field plane at 92 GHz; and (d) E-field plane at 92 GHz.

TABLE 2. FWHM and $1/e^2$ beam width extracted from measured images. The percentage difference in the extracted values from the camera image and EM simulated reference is given in brackets.

Camera Type	H-field Plane				E-field Plane			
	FWHM (mm)		$1/e^2$ (mm)		FWHM (mm)		$1/e^2$ (mm)	
	76 GHz	92 GHz	76 GHz	92 GHz	76 GHz	92 GHz	76 GHz	92 GHz
Reference HFSS Simulation (Raw)	12.4	10.6	23.0	20.1	12.3	10.7	22.9	19.8
Single-pixel Camera (Raw)	12.4 (0.4)	10.2 (3.8)	21.8 (4.9)	19.3 (4.0)	11.7 (4.9)	10.0 (6.5)	19.5 (14.8)	18.5 (6.6)
TeraSense (Proprietary Median-smooth Filter)	11.5 (7.0)	11.2 (5.7)	25.1 (9.3)	21.8 (8.5)	11.6 (5.8)	11.5 (7.4)	33.6 (46.8)	26.2 (32.3)
TeraSense (MATLAB 'Disk-smooth' Filter)	12.7 (2.9)	11.5 (8.5)	26.7 (16.4)	20.8 (3.5)	13.7 (10.7)	12.5 (17.2)	28.7 (25.4)	22.2 (12.1)

with simulations at both 76 GHz and 92 GHz. With the TeraSense camera, there is reasonable agreement with the use of its proprietary filter at both frequencies; the MATLAB filter giving a slightly better agreement with simulations.

Caution should be taken when extracting beam profile information using the TeraSense camera, even when using a smooth filter, due to poor image quality. Moreover, while the TeraSense camera is specified for operation down to 50 GHz, the difference performance for the $1/e^2$ beam widths in Table 2 is noticeably worse at 76 GHz, when compared to with the narrower beam 92 GHz.

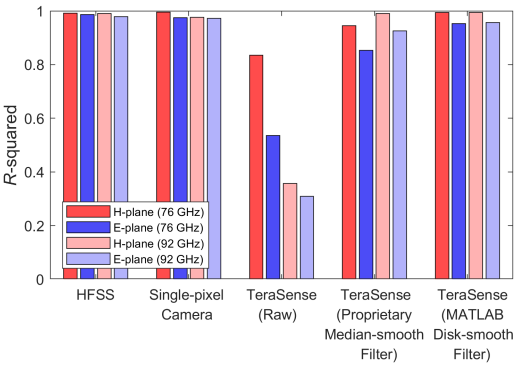

FIGURE 5. R-squared values for beam intensity profiles against the Gaussian approximation reference analytical model.

A reference analytical model is used to evaluate how accurately each camera captures H- and E-field plane beam cross section intensity distributions, in terms of overall shape, using statistical R-squared analysis. The analytical model assumes that the pyramidal horn antenna acts as a perfect Gaussian source, with a Gaussian approximation for beam intensity given by [19]:

$$I(r) = I_o \cdot e^{-2\left(\frac{r}{w_z}\right)^2} \tag{1}$$

where I_0 is peak beam intensity (or irradiance); r is the radial distance from the center axis of the beam; and w_z defines the beam radius at $1/e^2 \sim 13.5\%$ of its peak intensity (or $1/e$ of its peak field). From Table 2, the beam width $2w_z$ is taken from EM simulations and $I(r)/I_o$ is calculated against r, such that this analytical model can be compared directly against the plots in Fig. 4, to extract the R-squared values. The results are given in the bar chart shown in Fig. 5. Both the EM simulation and single-pixel camera images show a good fit to the Gaussian approximation for beam intensity. As expected, with the TeraSense camera, there is reasonable agreement with the use of its proprietary filter at both frequencies; the MATLAB filter giving a slightly better agreement with simulations.

B. COLLIMATED BEAM

With the diverging-beam, the peak beam intensity is relatively high (due to the short separation distance) and the $1/e^2$ beam width is only approximately 44% of the TeraSense camera aperture size, resulting in a large signal-to-noise ratio (SNR).

In this subsection, a collimated beam is used having a more complex profile and in a more challenging SNR environment. With an ideal single-point source and mirror (optical) assembly, geometric ray tracing shows that only one axis of symmetry exists (unlike the orthogonal two-axis symmetry for the diverging beam). Moreover, with the horn-mirror (quasi-optical) assembly, there will be additional distortion to the beam cross section to that found with the optical assembly. In addition, even small mechanical misalignments will add further distortion to the beam's cross-sectional profile.

With the same output power levels, the total separation distance is now increased from 30 mm to 246/346 mm and the

collimated $1/e^2$ beam widths are now of the same order as the TeraSense camera aperture size; resulting in a significantly degraded SNR. Moreover, with these larger beam widths, knife-edge diffraction from the front-facing aluminum casing around the aperture may cause further beam image distortion. Also, with any collimated beam, the effects of standing waves will become more pronounced from a camera having a high reflectance aperture. Two sets of images are taken at 76 GHz and 92 GHz, at different distances (170 mm and 270 mm) from the mirror along the propagation z-axis.

Figure 6 and Fig. 7 show the resulting images taken at separation distances of 170 mm and 270 mm, respectively. The single-pixel camera clearly shows the expected distortion in the beam cross section; as with the diverging beam, the $1/e^2$ beam widths at 92 GHz are noticeably smaller than at 76 GHz. In contrast, in this low SNR environment, the random noise adds to the existing problems of poor resolution and pixel quality, resulting in the TeraSense camera being unable to resolve the complex image seen by the single-pixel camera. For example, using only the raw image from the single-pixel camera, it can be seen that the $1/e^2$ beam widths slightly increase ($\sim$10% in the H-field plane and $\sim$1% in the E-field plane) as the separation distance increases from 170 mm to 270 mm; demonstrating that the beam is not perfectly collimated and that this assessment cannot be made with the TeraSense camera.

By observation of Fig. 6(c), 6(d), 7(c) and 7(d), pixels with high intensity values seen in raw TeraSense camera images are randomly distributed across the array. As a result, after applying the smooth filter, it becomes impossible to locate the beam center.

IV. STANDING-WAVE DETECTION

With the Tera-1024 camera, significant periodic fluctuations in the detected pixel power levels are observed when the camera is moved along the propagation z-axis. This phenomenon indicates the presence of standing waves between the camera and the source (also observed with the single-pixel camera, but to a lesser degree).

With a collimated beam, the spatial power intensity distribution is measured with both cameras. Each camera is moved along the propagation z-axis; 150 mm to 270 mm from the center of the 90° off-axis parabolic mirror. With the single-pixel camera, RAM is always used to minimize standing waves. Therefore, to observe its effectiveness, measurements are undertaken with and without the RAM. With the TeraSense camera, only the central pixel is chosen to record the power intensity.

Figure 8 shows the apertures for both cameras and Fig. 9(a) and 9(b) give the normalized propagation z-axis intensity distributions for the single-pixel camera with and without the RAM at 76 GHz and 92 GHz, respectively. It can be clearly seen that intensity has sinusoidal-type ripples along the propagation z-axis. At 76 GHz, the average distance between two peaks is measured as $\lambda_o/2 = 1.969$ mm, corresponding to a frequency of 76.1 GHz.

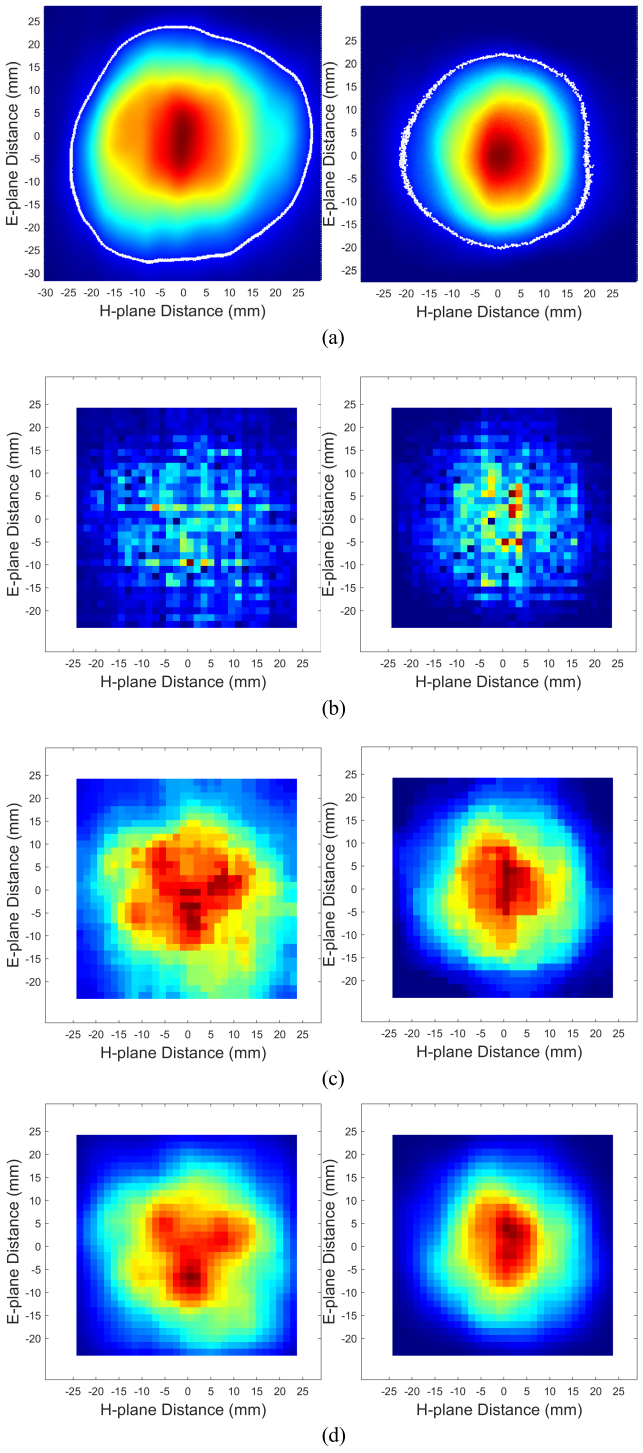

FIGURE 6. Measured collimating beam cross section images (normalized values) with a 170 mm separation distance between mirror center and camera aperture at 76 GHz (left) and 92 GHz (right): (a) single-pixel camera (raw); (b) TeraSense (raw); (c) TeraSense camera (proprietary median-smooth filter); and (d) TeraSense camera (MATLAB 'disk smooth' filter). The white loci represent the extracted $1/e^2$ boundaries.

Similarly, at 92 GHz, the average distance between two peaks is measured as $\lambda_o/2 = 1.634$ mm, corresponding to a frequency of 91.8 GHz. The RAM surrounding the aperture of the open-ended waveguide reduces the power intensity of the

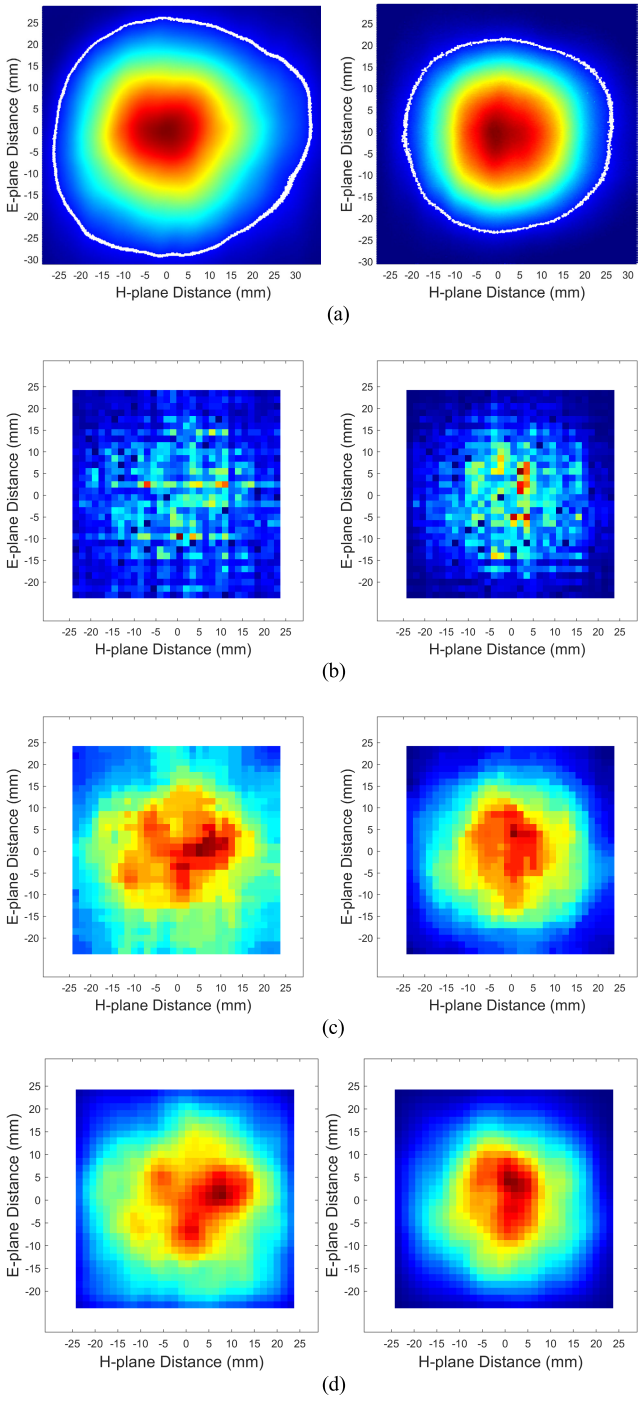

FIGURE 7. Measured collimating beam cross section images (normalized values) with a 270 mm separation distance between mirror center and camera aperture at 76 GHz (left) and 92 GHz (right): (a) single-pixel camera (raw); (b) TeraSense (raw); (c) TeraSense camera (proprietary median-smooth filter); and (d) TeraSense camera (MATLAB 'disk smooth' filter). The white loci represent the extracted $1/e^2$ boundaries.

standing wave by more than 3 dB. Figure 9(c) and 9(d) show normalized propagation z-axis intensity distributions for both cameras, over a zoomed-in range of 10 mm. At both 76 GHz and 92 GHz, the TeraSense camera show more prominent standing waves, when compared to the single-pixel camera with RAM and is of the same order without RAM.

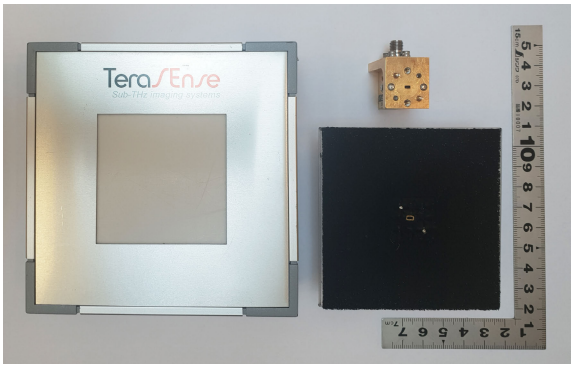

FIGURE 8. Photographs of the Tera-1024 camera with 48 mm × 48 mm aperture (left) and single-pixel camera detectors with 2.54 mm × 1.27 mm aperture (right) without (top) and with (bottom) RAM.

The voltage standing-wave ratio (VSWR) can, in principle, be read-off directly from Fig. 9. However, any extracted value for VSWR is meaningless since the source is also not impedance matched to that of the reference (impedance of free space η_o in our QO case). This will be found even with the most expensive commercially available vector network analyzers (VNAs), typically used as the source and detector, due to non-ideal components employed within the test set (irrespective of whether error correction is applied).

V. APERTURE REFLECTANCE MEASUREMENTS

Given the large standing waves, further investigation is required to quantify the power reflectance for both cameras. The two-sigma (i.e., $1/e^2$ normalized power) boundary for the collimated Gaussian beam (containing 95.45% of the beam power) projecting onto the TeraSense camera is commensurate in size with the square periphery of its FPA aperture. Also, in the previous section it was shown that the TeraSense camera creates significant standing waves. This should be of no surprise, as it is not possible to implement a conventional anti-reflection layer in front of ultra-broadband detectors.

In the US, the National Institute of Standards and Technology (NIST) undertook a reflectivity study of a target plastic sheet (12.94 mm thick Rexolite®, 1422 cross-inked polystyrene) at K-band (18 GHz to 26 GHz) [20]. Their target (having a reported dielectric constant of 2.55 and loss tangent of 6×10^{-4}) behaves as a Blackbody at the 3rd-order Fabry-Pérot resonance frequency of approximately 21.8 GHz, where the magnitude of its reflection coefficient is approximately zero. Here, Gu *et al.*, use a VNA and two-tier calibration process. First, a routine one-port calibration is performed, with a reference plane at the waveguide flange of their pyramidal horn antenna. Next, a few free-space calibration standards of known reflection coefficient are employed to correct for the free-space path loss of the diverging beam, impedance mismatch between free space and the Device Under Test (DUT), etc. [20]. Even with their commercial VNA and calibration routine, the corrected magnitude of reflection coefficient for a flat metal sheet exhibited a measured standing wave peak of 1.006 and trough of 0.996, over a one wavelength range,

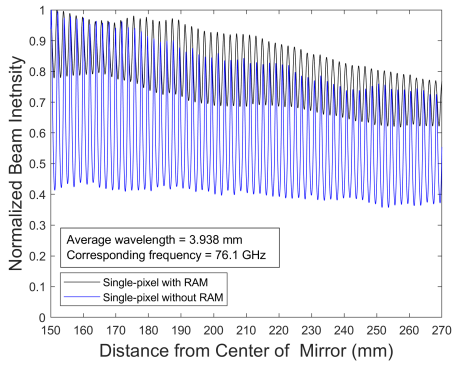

(a)

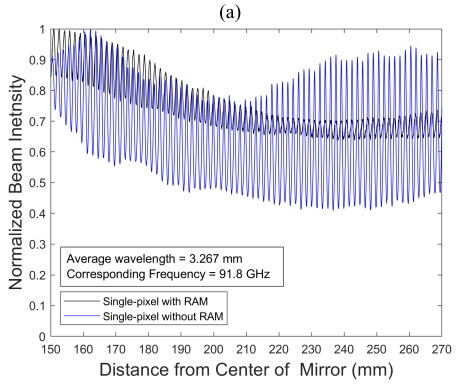

(b)

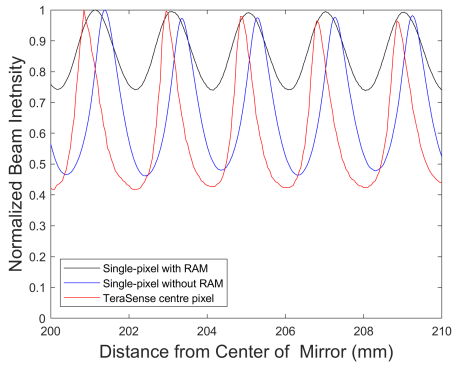

(c)

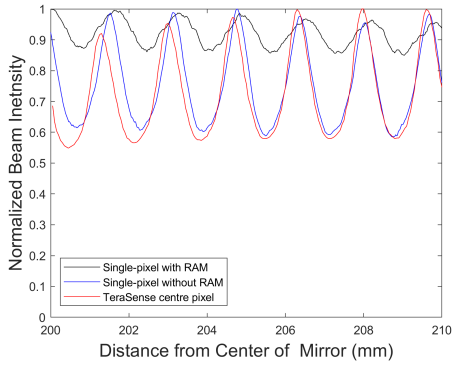

(d)

FIGURE 9. Beam intensity along the propagation z-axis (running average with 11 spatial points): (a) Single-pixel at 76 GHz; (b) Single-pixel at 92 GHz; (c) Both camera at 76 GHz (zoomed-in); and (d) Both cameras at 92 GHz (zoomed-in).

at a spot frequency of 18 GHz (corresponding to a reflectance peak).

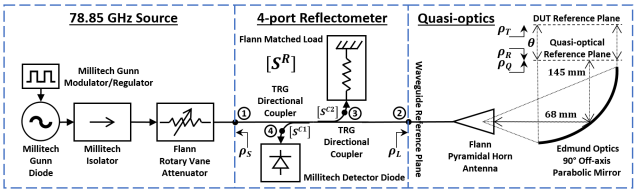

FIGURE 10. Detailed block-diagram of the bespoke W-band one-port quasi-optical scalar network analyzer.

This section will evaluate the level of power reflectance of the TeraSense camera's aperture, at a new spot frequency of 79 GHz. To this end, a simple bespoke one-port quasi-optical scalar network analyzer is developed.

A. W-BAND ONE-PORT QUASI-OPTICAL SCALAR NETWORK ANALYZER

The W-band one-port quasi-optical scalar network analyzer (1P-QO-SNA) is assembled using only commercially-available precision components, as illustrated by the detailed block diagram shown in Fig. 10; the complete system is shown in Fig. 11. Note that the TeraSense camera has a higher sensitivity to vertical E-field polarization and so this is taken into account by the orientation of the pyramidal horn antenna (Flann 27240-20, with gain of 18.7 dBi at 79 GHz [16]) that illuminates the 90° off-axis parabolic mirror to create the collimated incident beam. The camera is mounted on a 10 μm precision moveable stage, which provide both accuracy and repeatability. In order to minimize unwanted reflections during the reflectance measurements, RAM is added to cover the front-facing aluminum casing around the aperture. The separation distance between the antenna aperture and the center of the 90° off-axis parabolic mirror is dictated by the mirror's specified effective focal length of 76.2 mm. With the pyramidal horn antenna used, having a radiating aperture size of 12.4 mm × 9.0 mm (giving the largest dimension D_A = 15.32 mm), this distance is within the radiating near field; between the reactive near-field distance $z_{nf} = 0.62\sqrt{D_A^3/\lambda_o}$ (79 GHz) =19 mm and far-field distance $z_{ff} = 2D_A^2/\lambda_o$ (79 GHz) =124 mm, where λ_o = 3.797 mm is the wavelength in free space at 79 GHz. Within the collimated beam, the separation distance between the mirror and camera is not critical. In practice, however, if this distance is too short then the standing waves between the camera and the horn-mirror assembly can distort field pattern images displayed by the camera; while, if the distance is too large, the camera's SNR can be low, resulting in unacceptable image quality.

With reference to Fig. 10, at the center of the SNA is a four-port reflectometer, fed by a waveguide source and terminated by a quasi-optical load. With the former, a stable 79 GHz Gunn diode source (Millitech GDM-12 [12]) is employed with WR-12 to WR-10 transition, followed by an isolator (Millitech JFL-10-NI [12]), to reduce the inherent output impedance mismatch seen by the input of the reflectometer. A precision rotary vane attenuator (Flann 27110 [16]) is employed to limit the available output power from the source,

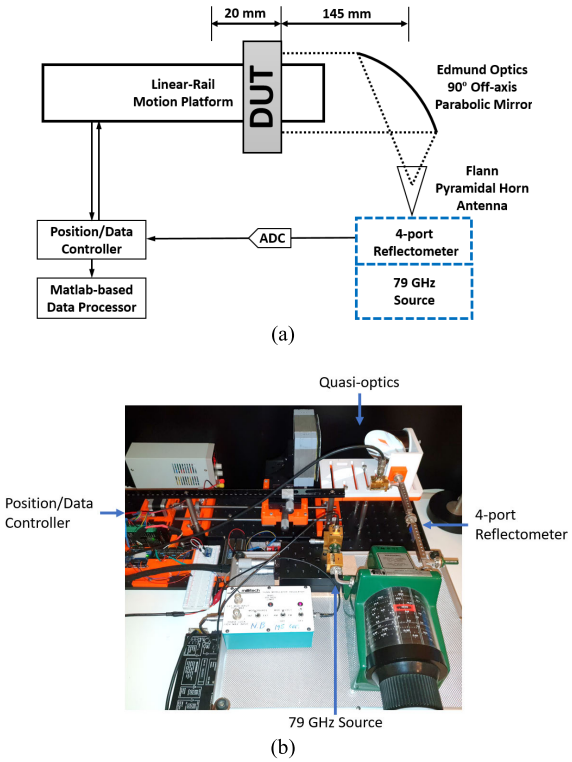

FIGURE 11. Complete W-band one-port quasi-optical scalar network analyzer system: (a) block diagram; and (b) photograph.

so as to avoid pushing the incident power detector out of its square-law region.

The source signal enters Port-1 and a fraction of this power is sampled and emerges from Port-3; the output voltage V_i from the square-law detector (connected to the coupled arm of the second -10 dB directional coupler) represents the power incident to the Waveguide Reference Plane. Similarly, the reflected signal enters Port-2 and a fraction of this power is sampled and emerges from Port-4; the output voltage V_r from the square-law detector (connected to the coupled arm of the first -10 dB directional coupler) represents the power reflected from the Waveguide Reference Plane.

The square-law detector (Millitech DXP-10 [12]) employs a high sensitivity, zero-bias, Schottky barrier beam lead diode. In practice, it is not possible to perfectly match the performance of any two detectors. Therefore, in order to minimize the introduction of errors with this four-port spectrometer, the same detector is used for both incident and reflected measurements; swapping them and terminating the other port with a dummy matched load (Flann 27040 [16]).

With reference to Fig. 11, for automated data collection and calibration, the DUT is placed on a motion platform (driven by a stepper motor and lead screw), which translates along the propagation z-axis (between 145 mm and 165 mm from the center of the 90° off-axis parabolic mirror). Similar to the data acquisition module for the single-pixel camera, the output voltage from the square-law detector is fed into an ADC and microcontroller (ATMEGA328). The stepper motor pauses approximately 0.5 seconds to ensure mechanical stability every 10 μm, and the microcontroller collects data (position and voltage). A custom MATLAB script is used to implement the bespoke calibration routines (discussed on following sections). As most of the measurement and calibration processes are automated, the Gunn diode modules can be replaced by a more sophisticated frequency swept source.

In Fig. 10, ρ_T is the target voltage-wave reflection coefficient at the DUT Reference Plane. In order to quantify the level of power reflectance $|\rho_T|^2$ from the TeraSense camera, in a quantitative way, it is necessary to fully-calibrate the bespoke 1P-QO-SNA system. As will be shown here, this undertaken with two very simple calibration steps that avoid the need to consider complex variables.

B. WAVEGUIDE REFLECTOMETER ANALYSIS

With reference to Fig. 10, the S-parameter matrices for the four-port reflectometer, first directional coupler and second directional coupler are $[S^R]$, $[S^{C1}]$ and $[S^{C2}]$, respectively; while the external voltage-wave reflection coefficients 'seen' by Port-1 (source) and Port-2 (load) are ρ_S and ρ_L, respectively.

At this point, it is important to first understand the subtle difference between what is measured by the four-port reflectometer and what can be inferred from the voltage standing-wave ratio at its measurement reference plane. For simplicity, remove the quasi-optical components (such that $\rho_L = e^{-j2\theta}\rho_T$) and let the four-port reflectometer be ideal and lossless. At the Waveguide Reference Plane, it can be shown that the respective normalized incident and reflected voltage waves v_{Li} and v_{Lr}, normalized voltage standing wave $v_L = v_{Li} + v_{Lr}$, $VSWR$ and the magnitude of the voltage-wave reflection coefficient can be represented as:

$$v_{Li} \Rightarrow S_{31}^R;\ v_{Lr} \Rightarrow S_{41}^R;\ v_L \Rightarrow S_{31}^R + S_{41}^R \tag{2}$$

$$|v_L|_{max} = |v_{Li}| + |v_{Lr}| \Rightarrow \left|S_{31}^R\right| + \left|S_{41}^R\right| \text{ and}$$

$$|v_L|_{min} = |v_{Li}| - |v_{Lr}| \Rightarrow \left|S_{31}^R\right| - \left|S_{41}^R\right| \tag{3}$$

and, therefore,

$$VSWR = \frac{|v_L|_{max}}{|v_L|_{min}} \Rightarrow \frac{\left|S_{31}^R\right| + \left|S_{41}^R\right|}{\left|S_{31}^R\right| - \left|S_{41}^R\right|} \neq f(\theta) \tag{4}$$

and,

$$|\rho_L| = \frac{VSWR - 1}{VSWR + 1} \neq f(\theta) \tag{5}$$

and, therefore,

$$|\rho_L| = \left|\frac{v_{Lr}}{v_{Li}}\right| \Rightarrow \left|\frac{S_{41}^R}{S_{31}^R}\right| \neq f(\theta) \tag{6}$$

Ideally, with $\rho_S = 0$, none of the expressions in (2)-(6) are a function of the displacement electrical length θ, between the Waveguide and DUT Reference Planes. However, if $\rho_S \neq 0$, all the voltage waves in (2)-(3) become a function of θ; by extension, this includes the measured voltages from the square-law detectors. This is because the 1P-QO-SNA system

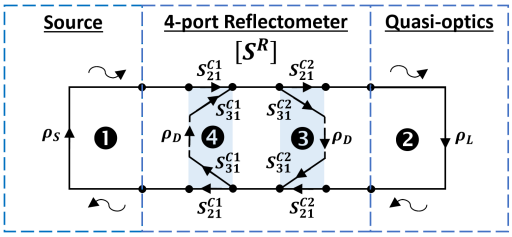

FIGURE 12. Simplified signal-flow graph of the four-port reflectometer.

essentially behaves as a one-dimensional resonator between the two reflecting boundaries ρ_S and ρ_T. Fortunately, taking the ratio of two similar voltage waves from (2)-(3), which have exactly the same ρ_S dependent denominator, will not result in *VSWR* and $|\rho_L|$ becoming a function of θ.

Now, consider the calibration of a practical reflectometer. In order to derive the closed-form expressions, it is first necessary to make some reasonable simplifying assumptions. Here, the commercial waveguide directional couplers and dummy matched load are assumed to be perfectly matched and that the isolation between the direct and coupled ports of the directional couplers are infinite; the resulting scenario is depicted by the signal-flow graph shown in Fig. 12. In practice, the directional coupler (Mi-Wave's 559W, previously TRG Division/Alpha Industries) has quoted typical directivity of 40 dB and main line return loss of -26.4 dB [21]; while the matched load has a quoted return loss better than -32.3 dB [16]; supporting our simplifying assumption.

With reference to Fig. 12, it can be shown that, using the heuristic engineering approach for vector voltage waves [22], the resulting S-parameters expressions (superscript R has been removed for clarity) are:

$$S_{31} = \frac{S_{21}^{C1} S_{31}^{C2}}{\Delta_{31}} \tag{7}$$

$$\Delta_{31} = 1 - \left(S_{21}^{C1}\right)^2 \rho_S \left[\left(S_{21}^{C2}\right)^2 \rho_L + \left(S_{31}^{C2}\right)^2 \rho_D\right] \tag{8}$$

$$S_{41} = \frac{S_{21}^{C1} \left(S_{21}^{C2}\right)^2 S_{31}^{C1} \rho_L}{\Delta_{41}} \tag{9}$$

$$\Delta_{41} = 1 - \left(S_{21}^{C2}\right)^2 \rho_L \left[\left(S_{21}^{C1}\right)^2 \rho_S + \left(S_{31}^{C1}\right)^2 \rho_D\right] \tag{10}$$

Now, since $\left|\left(S_{31}^{C1,2}\right)^2 \rho_D\right| \sim 0$ with -10 dB directional couplers, it will be found that:

$$\Delta \cong \Delta_{31} \cong \Delta_{41} \cong 1 - \left(S_{21}^{C1} S_{21}^{C2}\right)^2 \rho_S \rho_L \tag{11}$$

and, therefore,

$$\rho_L \cong \frac{S_{41}/S_{31}}{\left(S_{21}^{C2}\right)^2 S_{31}^{C1}/S_{31}^{C2}} \text{ and}$$

$$|\rho_L| \cong \frac{\sqrt{V_r/V_i}}{\left|\left(S_{21}^{C2}\right)^2 S_{31}^{C1}/S_{31}^{C2}\right|} \rightarrow \frac{\sqrt{V_r/V_i}}{0.84643} \text{ at 79 GHz} \tag{12}$$

TABLE 3. Bespoke 79 GHz one-port quasi-optical scalar network analyzer verification measurements.

Medium	Device Under Test	Source Attenuator Setting (dB)	Detector Voltages		Calibrated Measurements		Expected Return Loss (dB)
			V_i (mV)	V_r (mV)	Reflectance (%)	Return Loss (dB)	
Waveguide (Verification)	Short Circuit	20	9.26	6.71	101.1	+0.05	0.00
	Open-ended	10	65.1	2.85	6.110	-12.1	-13.9
	Matched Load	20	9.09	–	–	–	<-32.3 [16]
Quasi-optical	Horn – Free Space	0	308	0.23	0.104	-29.8	<-20.8 [16]
	Horn – Mirror – Free Space	0	338	0.34	0.140	-28.5	–

and for completeness,

$$S_{11} \cong \frac{\left(S_{21}^{C1} S_{21}^{C2}\right)^2 \rho_L}{\Delta} \text{ and } S_{22} \cong \frac{\left(S_{21}^{C1} S_{21}^{C2}\right)^2 \rho_S}{\Delta} \tag{13}$$

where, from W-band measurements of the non-ideal -10 dB ±1 dB directional couplers, the coupled values are $\left|S_{31}^{C1,2}(79\text{ GHz})\right| = [0.34993, 0.35154] \Rightarrow [-9.12, -9.08]$ dB and direct values are $\left|S_{21}^{C1,2}(79\text{ GHz})\right| = [0.91721, 0.92214] \Rightarrow [-0.75, -0.70]$ dB.

It is interesting to note that infinite transient reflections between Port-1 and Port-2 are included in the model, seen in (7)-(11). However, with reference to (12), this closed-loop path naturally disappears when determining the return loss $= 20log|\rho_L|$ measurements. Indeed, even with the impedance mismatched detector having $|\rho_D(79\text{ GHz})| = 0.75409 \Rightarrow$ -2.45 dB, $\left|\left(S_{31}^{C1,2}\right)^2 \rho_D\right| = [0.0923, 0.0932] \Rightarrow [-20.7, -20.6]$ dB at 79 GHz; justifying our approximations in (11)-(13). Moreover, neither the source reflection coefficient ρ_S or any phase information for the directional couplers are required. Of practical important, no calibration routine (requiring traceable waveguide standards) is required for the reflectometer part of the bespoke 1P-QO-SNA.

C. WAVEGUIDE REFLECTOMETER VERIFICATION MEASUREMENTS

To test the reflectometer part of the bespoke 1P-QO-SNA, it is first necessary to perform verification measurements at the Waveguide Reference Plane. Here, Flann waveguide short circuit and matched loads are employed [16]. The WR-10 waveguide, with its internal dimensions of 2.54 mm × 1.27 mm, have a theoretical ideal lossless cut-off frequency of 59.014 GHz and wave impedance of $\eta(79\text{ GHz}) = 1.508\eta_o$. As a result, an open-ended waveguide can also act as a convenient verification standard, having a theoretical reflection coefficient of $\rho_L(79\text{ GHz}) = 0.2025$, associated power reflectance of 4.10% and return loss of -13.87 dB. The results for these Waveguide Reference Plane verification measurements are given in Table 3.

Table 3 shows that the short circuit and open-ended waveguides gives 0.05 dB and 0.8 dB return loss errors, respectively. Due to detector noise, it is not possible to measure output

TABLE 4. Verification material sample modelling parameters.

Material Classification	Verification Material	Measured Thickness (μm)	Manufacturer Quoted DC Resistivity Range (ohm.cm)	Published Dielectric Constant	Extracted/ Published Loss Tangent x10⁴	First Fabry-Pérot Resonance Frequency (GHz)	Predicted Reflectance at 79 GHz (%)	Dielectric Parameter Reference Frequency (GHz)	Ref.
Semi-insulating (GaAs)	Undoped GaAs (100)	640	232,000,000 – 276,000,000	13.9876 (Extracted)	10 (Nominal)	65	61.2	97	–
Semiconducting (Silicon)	HRS (N-type)	385	3,500 – 5,000	11.67	5.8 – 4.1	115	62.3	82	[23]
	LRS (N-type)	510	5 – 10	11.7	4,043 – 2,022	86	13.8 –20.1		
	LRS (P-type)	480	0.8 – 1.2		25,269 – 16,846	–	46.3 – 54.7		
	LRS (N-type)	510	0.08 – 0.12		252,686 – 168,458	–	81.0 – 84.3		
Glass (Fused Quartz)	HOYA	1520	–	3.793	2.7	51	33.2	60	[24]
	JGS2	500				154	33.9		
Glass (Borosilicate)	BOROFLOAT®33	500		4.4	130	143	38.4	77	[25]
	Pyrex®	680		4.9	100	106	21.8	60	[26]
Plastic	Virgin PTFE G400-Guarniflon	2050		2.065	2.1	51	11.8	94	[27]
		1035				101	5.2		

voltages below ∼0.2 mV. As a result, the matched load could not be measured with any confidence (even with a 0 dB source attenuation setting). In addition to the previous validation measurements, the quasi-optical components placed *in situ* are also measured, with the pyramid horn antenna pointing at free space and also with the insertion of the parabolic mirror. As expected, it is found that the latter scenario degrades the performance of the former. Moreover, from the former, it is established that the reflectometer can perform measurements with a dynamic range between 30 dB and 32 dB.

The results presented here, for calibration standard-free measurements at the Waveguide Reference Plane, have validated the operation of the reflectometer part of the bespoke 1P-QO-SNA system. Next, it will be shown that a very simple calibration step can be applied to move the measurement reference plane from the Waveguide Reference Plane to the Quasi-optical Reference Plane. Finally, using another simple calibration step, the reference plane can be shifted from the Quasi-optical Reference Plane to the DUT Reference Plane.

D. WAVEGUIDE TO QUASI-OPTICAL REFERENCE PLANE SHIFT

At the Waveguide Reference Plane, using power propagation modeling [22], the reflectometer 'sees' the following:

$$|\rho_L|^2 \approx \left|\rho_L^{HM}\right|^2 + \eta_{HM}^2 \left|\rho_Q\right|^2 \text{ and}$$
$$\eta_{HM} \approx \left(1 - \left|\rho_L^{HM}\right|^2\right) G_{HM} \tag{14}$$

where, η_{HM} represents the overall efficiency of transferring power between the Waveguide Reference Plane and the Quasi-optical Reference Plane, associated with the horn-mirror (HM) assembly. This includes the impedance mismatch power loss factor $\left(1 - \left|\rho_L^{HM}\right|^2\right)$ and combined ohmic and optical misalignment power loss factor G_{HM}. Also, $\left|\rho_L^{HM}\right|^2$ represents the power reflectance from the HM assembly with no DUT target present (i.e., the collimated beam radiates into free space and without any returning reflections). In practice, $\left|\rho_L^{HM}\right| \approx 0$ and so $|\rho_L|^2 \sim \left|\rho_Q\right|^2$ with optically aligned commercial quasi-optical components. Nevertheless, for improved accuracy, the quasi-optical equivalent of a matched load measurement is undertaken to extract $\left|\rho_L^{HM}\right|^2$. Here, the measured horn-mirror assembly has $\left|\rho_L^{HM}\ (79\ \text{GHz})\right| = 0.03747 \Rightarrow$ -28.5 dB, as given in Table 3. In addition, the electromagnetic short circuit is measured, with a flat polished copper sheet positioned parallel and close to the quasi-optical reference plane. The average value of $\left|\rho_Q\right|^2$ as the position of this target is moved across a few standing wave cycles is $\left|\overleftrightarrow{\rho_Q}\right|^2 \cong 1$. The corresponding values of $|\rho_L|^2$ are measured and recorded to give an average value $\left|\overleftrightarrow{\rho_L}\right|^2$, so that G_{HM} can be extracted from:

$$G_{HM} \approx \frac{\sqrt{\left|\overleftrightarrow{\rho_L}\right|^2 - \left|\rho_L^{HM}\right|^2}}{\left(1 - \left|\rho_L^{HM}\right|^2\right)} \tag{15}$$

Finally, $\left|\rho_Q\right|^2$ can now be extracted directly from spectrometer measurements, such that:

$$\left|\rho_Q\right|^2 \approx \frac{|\rho_L|^2 - \left|\rho_L^{HM}\right|^2}{\eta_{HM}^2} \tag{16}$$

E. QUASI-OPTICAL TO DUT REFERENCE PLANE SHIFT

The following analysis assumes a perfectly collimated beam and with perfect optical alignment to achieve normal incidence to the DUT Reference Plane (having a voltage-wave reflection coefficient $\rho_T = |\rho_T|\, e^{j\angle\rho_T}$), physically separated by distance z and electrical length $\theta = 2\pi z/\lambda_o$ from the reflectometer's Quasi-optical Reference Plane (having a voltage-wave reflection coefficient $\rho_R = |\rho_R|\, e^{j\angle\rho_R}$). In the opposite direction, the Quasi-optical Reference Plane 'sees' the remote target with a voltage-wave reflection coefficient

$\rho_Q = |\rho_Q| e^{j\angle\rho_Q}$, such that:

$$\rho_Q = \frac{e^{-j2\theta}}{1 - \rho_R \rho_T e^{-j2\theta}} \cdot \rho_T \tag{17}$$

With an ideal planar reflecting sheet calibration target at the DUT Reference Plane has $\rho_T = -1$, implemented with a theoretical perfect electrical conductor (PEC), and the electromagnetic short circuit (SC) gives:

$$\left|\rho_Q^{SC}\right|^2 = \frac{1}{\left|1 + |\rho_R| e^{j\phi}\right|^2} \equiv \frac{1}{(1 + x_S)^2 + (y_S)^2} \tag{18}$$

where, $\phi = \angle\rho_R - 2\theta$, $x_S = |\rho_R| \cos\phi$ and $y_S = |\rho_R| \sin\phi$. By displacing the position of the short circuit by a $\lambda_o/4$ offset, the resulting offset short (OS) gives:

$$\left|\rho_Q^{OS}\right|^2 \equiv \frac{1}{(1 - x_S)^2 + (y_S)^2} \tag{19}$$

where,

$$y_S = \sqrt{\frac{1}{\left|\rho_Q^{SC}\right|^2} - (1 + x_S)^2} \text{ and}$$

$$x_S = \frac{1}{4}\left(\frac{1}{\left|\rho_Q^{SC}\right|^2} - \frac{1}{\left|\rho_Q^{OS}\right|^2}\right) \tag{20}$$

giving,

$$|\rho_R|^2 = (x_S)^2 + (y_S)^2 = \frac{1}{2}\left(\frac{1}{\left|\rho_Q^{SC}\right|^2} + \frac{1}{\left|\rho_Q^{OS}\right|^2}\right) - 1 \tag{21}$$

With a DUT target (TA) at the DUT Reference Plane:

$$\left|\rho_Q^{TA}\right|^2 = \frac{|\rho_T|^2}{\left|1 - |\rho_R|\,|\rho_T|\, e^{j\psi}\right|^2} \equiv \frac{|\rho_T|^2}{(1 - x_T)^2 + (y_T)^2} \tag{22}$$

where, $\psi = \phi + \angle\rho_T$, $x_T = |\rho_R|\,|\rho_T| \cos\psi$ and $y_T = |\rho_R|\,|\rho_T| \sin\psi$. By displacing the position of the target by a $\lambda_o/4$ offset, the resulting offset target (OT) gives:

$$\left|\rho_Q^{OT}\right|^2 \equiv \frac{|\rho_T|^2}{(1 + x_T)^2 + (y_T)^2} \tag{23}$$

where,

$$y_T = \sqrt{\frac{|\rho_T|^2}{\left|\rho_Q^{TA}\right|^2} - (1 - x_T)^2} \text{ and}$$

$$x_T = \frac{|\rho_T|^2}{4}\left(\frac{1}{\left|\rho_Q^{OT}\right|^2} - \frac{1}{\left|\rho_Q^{TA}\right|^2}\right) \tag{24}$$

giving,

$$|\rho_R|^2\,|\rho_T|^2 = (x_T)^2 + (y_T)^2 = \frac{|\rho_T|^2}{2}\left(\frac{1}{\left|\rho_Q^{TA}\right|^2} + \frac{1}{\left|\rho_Q^{OT}\right|^2}\right) - 1 \tag{25}$$

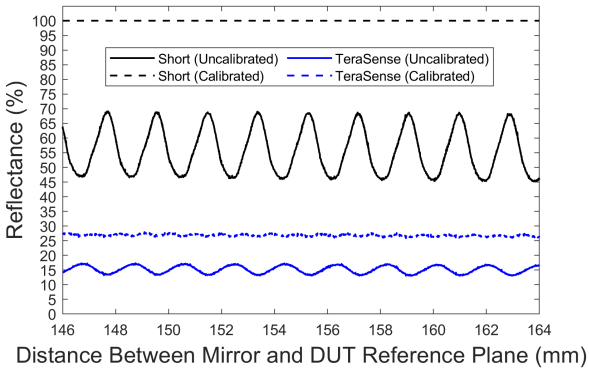

FIGURE 13. Measured reflectance for the flat copper calibration and TeraSense aperture targets, with and without calibration, over a range of approximately five wavelengths at 78.85 GHz (no running average).

and, therefore,

$$|\rho_T|^2 = \frac{(x_T)^2 + (y_T)^2}{(x_S)^2 + (y_S)^2} = \frac{2}{\left(\frac{1}{\left|\rho_Q^{TA}\right|^2} - \frac{1}{\left|\rho_Q^{SC}\right|^2} + \frac{1}{\left|\rho_Q^{OT}\right|^2} - \frac{1}{\left|\rho_Q^{OS}\right|^2}\right) + 2} \tag{26}$$

The copper sheet calibration and DUT targets are located such that standing-wave peak values of V_r are measured, giving $\left|\rho_Q^{SC}\right|^2$ and $\left|\rho_Q^{TA}\right|^2$, respectively. The $\lambda_o/4$ offset locations can then be easily found by obtaining adjacent standing-wave trough values of V_r, giving $\left|\rho_Q^{OS}\right|^2$ and $\left|\rho_Q^{OT}\right|^2$. In practice, using our automated data collection routine, measurements were collected across approximately five wavelengths. Within this dataset, (26) was calculated for every possible pair of data points with quarter-wavelength separation and then averaged. Note that the copper calibration and DUT targets only need to be approximately in the same locations (i.e., within a few wavelengths relative to each other), without any significant loss of accuracy.

The reflectance for the flat copper sheet calibration target, with and without correction, is shown in Fig. 13, with increasing distance between the parabolic mirror and DUT reference plane. As shown in Fig. 13, the corrected reflectance for the short must always be 100%, by definition, in accordance with (26). Moreover, from the uncorrected reflectance of the short, the incident beam appears to be collimated across the displacement range of 18 mm.

F. MODELING AND MEASUREMENT OF VERIFICATION MATERIAL SAMPLES

The performance of the complete bespoke 1P-QO-SNA system can be verified using verification material sample targets. The caveat for any verification procedure is that both the physical and electrical characteristics of the material samples are accurately known *a priori*.

The verification material samples consist of a mixture of optically-polished semiconductor and glass wafers, as well

as plastic sheets, having a measured thickness l, such that only the first Fabry-Pérot resonance frequency is below the 79 GHz operating frequency. Table 4 lists the verification materials used and their modeling parameters, to provide sufficient traceability for our needs.

The voltage-wave reflection coefficient, for a collimated beam at normal incidence to an optically flat material under test that is large enough not to exhibit significant diffraction effects, and associated Fabry-Pérot resonance frequencies f_{FP} can be calculated from the following expressions [22]:

$$\rho_T = \frac{1 - e^{-2\gamma l}}{1 - \left(\rho_0 e^{-\gamma l}\right)^2} \cdot \rho_0 \text{ and } f_{FP} \cong N\frac{c}{2nl} \tag{27}$$

where, $\rho_0 = (1-\tilde{n})\,/\,(1+\tilde{n})$ is the zero-order electric-field wave reflection coefficient for the material under test located in free space; $\gamma = j\beta_o\tilde{n}$ is the propagation constant; β_o is the phase constant in free space; $\tilde{n} = \sqrt{\varepsilon'_{reff}\,(1 - jtan\delta)}$ is the complex refractive index for a non-magnetic material; ε'_{reff} and $tan\delta$ are the respective real part of the complex effective relative permittivity (i.e., dielectric constant) and effective loss tangent; $n = \mathcal{R}\{\tilde{n}\}$ is the refractive index; c is the speed of light in free space; and $N \in [1, 2, 3 \ldots \infty]$ is the order of the Fabry-Pérot resonance frequency.

The complex effective relative permittivity is given by:

$$\tilde{\varepsilon}_{reff} = \varepsilon'_{reff} - j\varepsilon''_{reff} = \tilde{\varepsilon}_r - j\frac{\tilde{\sigma}}{\omega\varepsilon_0} \text{ and } tan\delta = \frac{\varepsilon''_{reff}}{\varepsilon'_{reff}} \tag{28}$$

where, $\tilde{\varepsilon}_r = \varepsilon'_r - j\varepsilon''_r$ represents the complex relative permittivity associated with the dielectric properties of the material, while $\tilde{\sigma} = \sigma' - j\sigma''$ represents the complex conductivity associated with the free carriers inside the material; $\sigma' = 1/\varrho_0$, where ϱ_0 is the DC resistivity for a semiconducting wafer, and ε_0 is the permittivity of free space. With semiconductor wafers, $\varepsilon''_r \approx 0$ and $\sigma'' \cong 0$ below terahertz frequencies [28] and so the dielectric constant is effectively independent of the wafer's resistivity. As a result:

$$\varepsilon'_{reff} \cong \varepsilon'_r \text{ and } tan\delta \cong \left(\frac{\varepsilon''_r}{\varepsilon'_r} + \frac{1}{\omega\varepsilon_0\varepsilon'_r\varrho_0}\right) \approx \frac{1}{\omega\varepsilon_0\varepsilon'_r\varrho_0} \text{[28]} \tag{29}$$

Blonde *et al.* [28] reported a constant value of $\varepsilon'_{reff} = 11.55$ for a high-resistivity silicon (HRS) wafer having $\varrho_0 \sim 6.8\ \text{k}\Omega \cdot \text{cm}$, extracted from whispering gallery dielectric resonator modes between 90 GHz and 96 GHz, and then used this to predict $tan\delta$ across W-band; effectively $\varepsilon'_{reff} \neq f(\sigma'', \varrho_0, \omega)$ and $\omega tan\delta \neq f(\varepsilon''_r, \sigma'', \omega)$. Note that this value of dielectric constant is much lower than the low frequency textbook value of 11.68. In practice, power reflectance and return loss can be very sensitive to even relatively small errors in dielectric constant, especially at an operating frequency close to Fabry-Pérot resonance frequencies and with large values of ϱ_0. However, Afsar and Button published precise spectroscopic data for a HRS wafer having $\varrho_0 \sim 8\ \text{k}\Omega \cdot \text{cm}$; with $\varepsilon'_{reff}(100\ \text{GHz}) = 11.67725$ and $tan\delta(100\ \text{GHz}) \times 10^4 = 19 \approx 10^4/\omega\varepsilon_0\varepsilon'_{reff}(100\ \text{GHz})\varrho_0 \sim 22$ [29]. More recently, Afsar and Chi reported similar values for HRS wafers with $\varrho_0 \sim 2$ & $1.5\ \text{k}\Omega \cdot \text{cm}$, having respective values of $\varepsilon'_{reff}(100\ \text{GHz}) = 11.678$ & 11.697 and $tan\delta(100\ \text{GHz}) \times 10^4 = 17.5$ & $17.5 \approx 10^4/\omega\varepsilon_0\varepsilon'_{reff}(100\ \text{GHz})\varrho_0 \sim 7.7$ & 10.2 [23]. Similarly, at 82 GHz, $\varepsilon'_{reff}(82\ \text{GHz}) = 11.6719$ & 11.7068 and $tan\delta(82\ \text{GHz}) \times 10^4 = 21.5$ & $20.4 \approx 10^4/\omega\varepsilon_0\varepsilon'_{reff}(82\ \text{GHz})\varrho_0 \sim 9.4$ & 12.5 [23]. Fortunately, power reflectance and return loss are relatively insensitive to small errors in loss tangent, even at frequencies close to Fabry-Pérot resonances and with high values of ϱ_0.

An extremely high purity semi-insulating GaAs wafer is used as a verification material sample, as this is used as the substrate for the TeraSense FPA. Previously reported values for dielectric constant and loss tangent are not used [29], [30]. The next subsection explains the reason for this and describes the method used for extracting the dielectric constant for a high purity GaAs wafer.

Finally, two different types of glass wafers (fused quartz and borosilicate) and two plastic sheets of white PTFE with different thicknesses also acted as verification material samples. White PTFE is chosen as it is also used as the protective cover for the TeraSense camera [5]. Indeed, the surface texture of our non-optically flat samples appear to match the protective cover.

Note that, in the UK, the National Physical Laboratory (NPL) recently characterized HRS and PTFE at V-band (50 GHz to 75 GHz), using a commercial VNA and a separate material characterization kit (MCK) [31]. Within V-band, the 4$^{\text{th}}$- and 5$^{\text{th}}$-order Fabry-Pérot resonance frequencies of the 3.06 mm thick HRS sample are captured; while the 3$^{\text{rd}}$- and 4$^{\text{th}}$-order are captured by the 5.99 mm thick PTFE sample. Unfortunately, the DC resistivity is not quoted for HRS, while the type of PTFE is also not mentioned. As a result, their extracted values for dielectric constant and loss tangent at 75 GHz could not be used, although they are commensurate with those given in Table 4.

The predicted and measured reflectance values for these flat verification material samples are shown in Table 4 and Fig. 14. It can be clearly seen that good agreement is found with all the samples, verifying the satisfactory operation of the complete bespoke 1P-QO-SNA system.

G. MODELING AND MEASUREMENT OF GaAs MIRROR

The TeraSense camera detector sensitivity decreases monotonically with increasing frequency when a silicon lens is added; this effectively embeds the detector within a semi-infinite substrate, by suppressing Fabry-Pérot reflections at the silicon-GaAs boundary [3].

However, without this lens (i.e., the camera pixel is located *in situ* at the air-GaAs boundary [3]), the frequency response of the detector sensitivity will have spectral peaks and troughs. In practice, a thermally evaporated metallic reflector is deposited onto the backside of the GaAs wafer [3]; this grounded dielectric slab acts as a GaAs mirror. As a result, at the front (active) side of the GaAs wafer, there is destructive

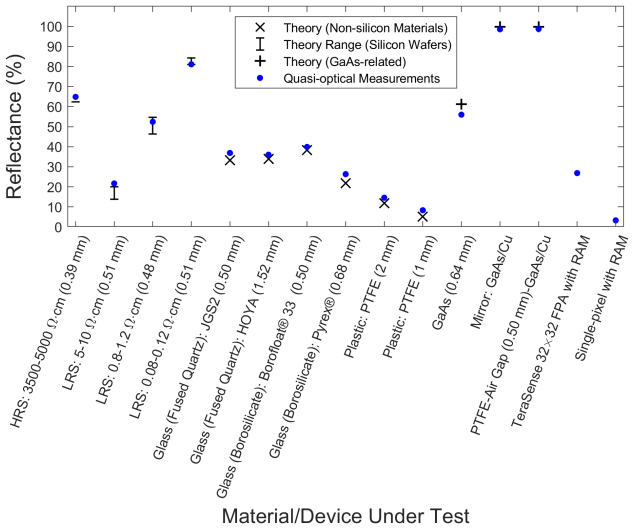

FIGURE 14. Predicted and measured verification materials and devices under test at 79 GHz.

(electromagnetic short circuit, SC) and constructive (electromagnetic open circuit, OC) interference at the following frequencies:

$$f_{SC} \cong N\frac{c}{2nl_2} \text{ and } f_{OC} \cong \left(N-\frac{1}{2}\right)\frac{c}{2nl_2} \tag{30}$$

where $n \cong \sqrt{\varepsilon'_{reff}}$ is the refractive index for the semi-insulating GaAs wafer; l_2 is the thickness of the GaAs mirror (quoted as 620 μm [3]), and $N \in [1, 2, 3 \ldots \infty]$ is the order of interference (i.e., order of Fabry-Pérot resonance frequency). From the peaks in detector sensitivity, Shchepetilnikov *et al.* fit a linear curve for Δf_{OC} against $1/l_2$, extracting an estimated aggregate value of $n = 3.8$ for various GaAs wafer thicknesses (used to spectrally tune detector sensitivity); stating that this value of refractive index is in good agreement with the value reported in literature [29], [32]. However, at room temperature, Afsar and Button [30] shows values that generally decrease from 3.5944 to 3.5854 as frequency increases from 75 GHz to 400 GHz; while Marple shows values increasing from 3.36 and 3.60 as frequency increases from 175 THz and 330 THz.

Clearly, there is a significant discrepancy in refractive index, between 3.8 reported by Shchepetilnikov *et al.* and previously reported maximum values of 3.6 [29], [32]. To some extent, this discrepancy can be attributed to the combined uncertainties associated with the optical path length product nl_2 in (30). For example, with two independently supplied Cr-doped single-crystal semi-insulating GaAs samples, having DC resistivities of 50 M$\Omega \cdot$ cm and 78 M$\Omega \cdot$ cm, Afsar and Button showed that (in addition to decreasing ε''_{reff}) a higher DC resistivity increases ε'_{reff} and n [29], [30]; with today's high purity crystal growth techniques, our undoped GaAs wafer has a manufacturer's quoted resistivity of 250 M$\Omega \cdot$ cm and, therefore, it is expected that $n > 3.6$. Also, GaAs wafer thickness is difficult to control and the physical measurement of l_2 will have associated tolerances. For example, a micrometer screw gauge with Vernier scales can have accuracy values from ± 1 μm upwards, depending on its quality, and this can be a potential source of significant error with lower quality gauges. Another potential contribution to the discrepancy is the influence that the log-periodic antenna has on the detector sensitivity peak frequencies. Finally, the accuracy of determining the detector sensitivity peak frequencies, especially with noisy measurements, with have associated uncertainties.

Assuming that the only significant contribution to any discrepancy in the value of refractive index is due to the higher purity of the GaAs, a manual extraction will now be undertaken using the reported detector sensitivity peaks with their 620 μm wafer [3].

The voltage-wave reflection coefficient, at normal incidence to an optically flat mirror (with PEC backside reflecting layer) that is large enough not to exhibit diffraction effects from the collimated beam, can be calculated from the following expression [22]:

$$\rho_{MIRROR}^{PEC} = \frac{\rho_0 - e^{-2\gamma l}}{1 - \rho_0 e^{-2\gamma l}} \tag{31}$$

For a wafer thickness of exactly 620 μm, it will be shown in the next subsection that there is an excellent match between the spectral peaks in detector sensitivity (reported at $N \in [2, 3, 4, 5, 6, 9, 10, 11]$) and the associated constructive interference with $n(N) \in [3.74, 3.55, 3.74, 3.67, 3.68, 3.70, 3.70, 3.70]$, highlighting the frequency dispersive nature of this material system (nominally with $n \approx 3.7$ across the 50 GHz to 700 GHz frequency range), exhibiting spectral dips in reflectance at $f_{OC}(N) \approx [97, 170, 226, 296, 361, 555, 621, 686]$ GHz. From these datasets, $n(2) = 3.74$ gives the extracted value of $\varepsilon'_{reff}(97 \text{ GHz}) = 13.9876$ found in Table 4. This value of dielectric constant is used to predict the reflectance at 79 GHz for the GaAs verification material sample, GaAs mirror and the more complicated PTFE Cover-Air Gap-GaAs Mirror material system, with all results shown in Fig. 14.

The bespoke 1P-QO-SNA system is used to measure a 640 μm thick semi-insulating GaAs wafer attached to a polished flat copper reflecting backplane, in an attempt to create an ideal GaAs mirror. As shown in Fig. 14, the predicted and measured reflectance values at 79 GHz are 99.73% and 98.50%. The 1.23% discrepancy can be attributed, in part, to the use of copper instead of the modeled PEC reflector; with an intrinsic impedance $\eta_{CU}(79 \text{ GHz}) \cong 73.2(1+j)$ m$\Omega/\square$ [33], at room temperature, a flat bulk copper sheet has a reflection coefficient of $-0.9996 + j0.0004 \cong -1$ and reflectance of 99.92% at 79 GHz – this justifies the use of our PEC approximation.

H. MODELING AND MEASUREMENT OF PTFE COVER-AIR GAP-GaAs MIRROR MATERIAL SYSTEM

Having established a means of accurately characterizing the GaAs mirror, the next step is to investigate the effects of using a PTFE protective cover for the GaAs mirror, as found with the TeraSense camera [5]. To this end, an exact analysis for

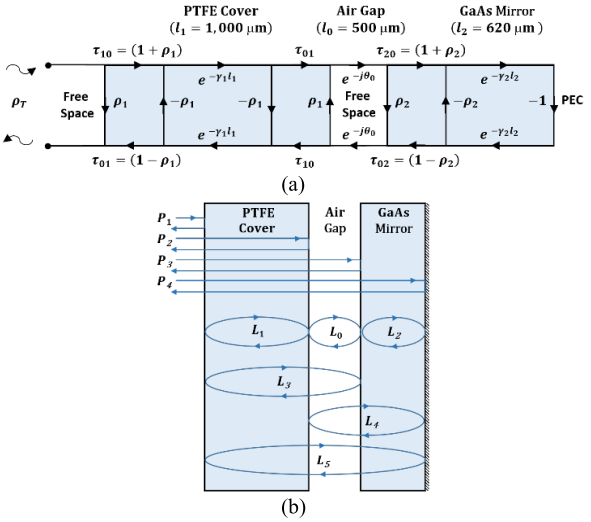

FIGURE 15. Analytical representations for the ideal PTFE Cover-Air Gap-GaAs Mirror material system: (a) signal-flow graph; and (b) identification of all reflection paths (*Px*) and internal loops (*Lx*).

the ideal PTFE Cover-Air Gap-GaAs Mirror must be undertaken. The analytical representations of this more complex material system is shown in Fig. 15.

From Fig. 15, using Mason's non-touching loop rule, it can be shown that the exact voltage-wave reflection coefficient at the front surface of the PTFE cover is given by (32), as shown at the bottom of the page.

where,

$$P_1 = \rho_1;\ P_2 = -\rho_1\left(1-\rho_1^2\right)e^{-2\gamma_1 l_1};$$
$$P_3 = \rho_2\left(1-\rho_1^2\right)^2 e^{-2(\gamma_1 l_1 + j\phi_0)}$$
$$P_4 = -\left(1-\rho_1^2\right)^2\left(1-\rho_2^2\right)e^{-2(\gamma_1 l_1 + j\phi_0 + \gamma_2 l_2)} \quad (33)$$

and,

$$L_0 = \rho_1\rho_2 e^{-j2\phi_0};\ L_1 = \rho_1^2 e^{-2\gamma_1 l_1};$$
$$L_2 = \rho_2 e^{-2\gamma_2 l_2};\ L_3 = -\rho_1\rho_2\left(1-\rho_1^2\right)e^{-2(\gamma_1 l_1 + j\phi_0)}$$
$$L_4 = -\rho_1\left(1-\rho_2^2\right)e^{-2(j\phi_0+\gamma_2 l_2)};$$
$$L_5 = \rho_1\left(1-\rho_1^2\right)\left(1-\rho_2^2\right)e^{-2(\gamma_1 l_1 + j\phi_0 + \gamma_2 l_2)} \quad (34)$$

and,

$$\rho_1 = \frac{1-\tilde{n}_{PTFE}}{1+\tilde{n}_{PTFE}};\ \gamma_1 = j\frac{2\pi}{\lambda_o}\tilde{n}_{PTFE};$$
$$\phi_0 = \frac{2\pi}{\lambda_o}l_0;\ \rho_2 = \frac{1-\tilde{n}_{GaAs}}{1+\tilde{n}_{GaAs}};\ \gamma_2 = j\frac{2\pi}{\lambda_o}\tilde{n}_{GaAs} \quad (35)$$

where, the complex refractive index $\tilde{n}$ of the PTFE and GaAs are related to their values of dielectric constant and loss tangent by $\tilde{n} = \sqrt{\varepsilon'_{reff}}\,(1 - jtan\delta)$. Setting $\tilde{n}_{PTFE} \to 1$ and $l_1, l_0 \to 0$ essentially removes the protective cover and (32) becomes (31). The simulated spectral responses for the 1 mm thick PTFE cover (red curves), 620 μm thick GaAs mirror (blue curve) and their combination with a 0.5 mm air gap [5] (black curve) is shown Fig. 16.

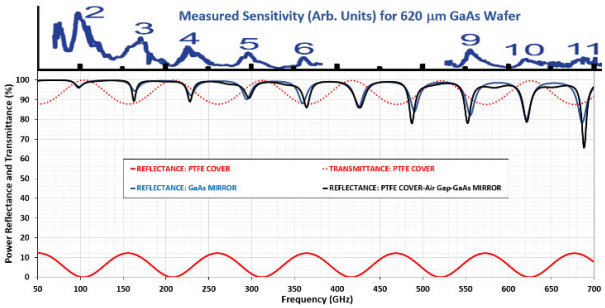

FIGURE 16. Simulated responses for 1 mm thick PTFE cover, 620 μm thick GaAs mirror (nominal values of $n = 3.7$ and $tan\delta = 10\times10^{-4}$) and PTFE Cover-Air Gap-GaAs Mirror material system. The measured detector sensitivity [3] is shown above.

As shown in Fig. 16, with nominal values of $n = 3.7$ and $tan\delta = 10 \times 10^{-4}$ across the certified (50 GHz to 700 GHz) spectral range of the TeraSense camera [5], the 620 μm thick semi-insulated GaAs mirror exhibits high reflectance; with broad peaks at $f_{SC}(N)$, ranging between 98-100%. The sharper dips at $f_{OC}(N)$ can be seen to line-up with the measured peaks in detector sensitivity [3]. Moreover, the depths of these reflectance dips and reduction in detector sensitivity peaks both increasing with frequency. The PTFE cover (in isolation) exhibits almost perfect destructive interference troughs in reflectance, giving more than 99.5% transmittance at these Fabry-Pérot resonance frequencies [34], due to the low loss nature of PTFE at sub-THz frequencies. Moreover, with worst-case peak reflectance values of 12%, the corresponding worst-case transmittance is 88% (i.e., insertion loss of only -0.555 dB); with a 6.20% reflectance and 93.76% transmittance at 79 GHz. When combined with the GaAs mirror, the reflectance of the mirror dominates that of the cover in isolation.

The bespoke 1P-QO-SNA system is used to measure our PTFE Cover-Air Gap-GaAs Mirror material system, to emulate the basic construction of a camera. As shown in Fig. 15, the predicted and measured reflectance values at 79 GHz are 99.76% and 98.73%. Here, the 1% discrepancy can again be attributed, in part, to the practical use of copper instead of the modeled PEC reflector

I. MEASUREMENT OF TERA-1024 AND SINGLE-PIXEL CAMERA APERTURE

In practice, unlike the over-simplified ideal modeling undertaken in the previous subsection, any two-dimensional array

$$\rho_T = P_1 + \frac{P_2\left[1-(L_0+L_2+L_4)+(L_0L_2)\right]+P_3\left(1-L_2\right)+P_4}{1-(L_0+L_1+L_2+L_3+L_4+L_5)+(L_0L_1+L_0L_2+L_1L_2+L_1L_4+L_2L_3)-(L_0L_1L_2)} \quad (32)$$

of log-periodic antennas will ultimately dominate the overall reflectance seen at the front surface of the TeraSense camera. Nevertheless, having established an accurate means of measuring power reflectance with the bespoke 1P-QO-SNA system, the Tera-1024 camera (having RAM covering the front-facing aluminum casing) performance will be compared with the single-pixel camera. As shown in Fig. 15, the measured reflectance values for both cameras are 26.9% and 3.3% at 79 GHz. Clearly, the TeraSense camera (with additional RAM) has a very significant level of reflectance at 79 GHz, albeit much lower than the 98.7% reflectance found with our simple PTFE Cover-Air Gap-GaAs Mirror material system. The reduction, from 98.7% to 26.9% could be explained by the complete 32 × 32 pixel array being in parallel with the surface impedance of the GaAs mirror [35]. In contrast, as expected, the single-pixel camera has insignificant reflectance at 79 GHz.

It is worth mentioning that when the 79 GHz Gunn diode source is replaced with one operating at 92 GHz (Millitech GDM-10 [12]), preliminary measurements show that the TeraSense camera has a reflectance of 29% at 92 GHz; as expected, indicating a low level of frequency dispersion over the relatively small increase in spot frequency.

VI. CONCLUSION

This is the first time the characteristics of an evolving commercial camera technology that can operate at millimeter-wave frequencies has been independently investigated. Here, we benchmark the TeraSense camera against a custom-built single-pixel camera at W-band, for image quality and aperture reflectance.

When compared to a reference single-pixel camera, the TeraSense camera exhibits limited image resolution and fidelity, with significant levels of systematic spatial noise (due to faulty pixels and high pixel-to-pixel responsivity deviation). In a poor signal-to-noise scenario, the addition of random noise exacerbates the problems with poor resolution and pixel quality. While the TeraSense camera technology can provide a convenient means of measuring beam profiles at room temperature, in low SNR environments poor image quality prohibits accurate characterization. We have identified possible causes of both beam and image distortion; this gives important insight into the best use of (sub-)THz cameras and interpretation of their images.

The inherent standing waves caused by the significant power reflectance of the camera aperture has been investigated in detail. A simple W-band one-port quasi-optical scalar network analyzer is developed, to determine the levels of reflectance for both cameras, with its bespoke calibration routine derived from first principles. This has been validated using a mix of traceable semiconductor and glass wafers, as well as plastic sheets. This simple scalar measurement system can be adapted to other bands and implementation technologies (i.e., not just with rectangular waveguide and free-space quasi-optics) – providing a low-cost solution for many non-destructive testing applications.

It is found that the TeraSense camera (with additional RAM) and single-pixel camera (having default RAM) have measured reflectance values of 27% and 3%, respectively, over a corresponding aperture area ratio of approximately 714:1; clearly illustrating the inherent problem of standing waves with broadband FPA cameras. While our custom-made non-pre-amplified direct-detection single-pixel camera provides excellent image resolution and fidelity, it inherently suffers from very slow raster-scanning speeds and operational bandwidth limitations. For this reason, the TeraSense camera technology is excellent for performing qualitative measurements in real time, with the caveats outlined in this paper.

ACKNOWLEDGMENT

The authors would like to thank R. Cheng for his help with faulty pixel mapping and R. Sloan at Microwave Inspection Technologies Limited (U.K.) for useful discussions on this work. Finally, the first author would like to sincerely thank Y.-H. Cheng for all the logistical support for this work during the COVID-19 lockdown.

REFERENCES

[1] J. Sun, F. Hu, and S. Lucyszyn, "Predicting atmospheric attenuation under pristine conditions between 0.1 and 100 THz," *IEEE Access*, vol. 4, pp. 9377–9399, Nov. 2016.

[2] I. Kukushkin and V. Muravev, "Apparatus and method of detecting electromagnetic radiation," U.S. Patent US8 772 890 B2, Jul. 8, 2014.

[3] A. V. Shchepetilnikov, B. D. Kaysin, P. A. Gusikhin, V. M. Muravev, G. E. Tsydynzhapov, A. Yu Nefyodov, A. A. Dremin, and I. V. Kukushkin, "Optimization of the frequency response of a novel GaAs plasmonic terahertz detector," *Opt. Quantum Electron.*, vol. 51, p. 376, Nov. 2019.

[4] V. M. Muravev, P. A. Gusikhin, I. V. Andreev, and I. V. Kukushkin, "Novel relativistic plasma excitations in a gated two-dimensional electron system," *Phys. Rev. Lett.*, vol. 114, no. 10, pp. 1–5, Mar. 2015.

[5] *TeraSEnse Sub-THz Imaging Systems, User Manual, Revision 1.6*. Accessed: Oct. 14, 2020. [Online]. Available: https://terasense.com/downloads/Terasense/Terasense%20T15%20Manual-1.6.pdf

[6] S. Lucyszyn, X. Shang, W. J. Otter, C. W. Myant, R. Cheng, and N. M. Ridler, "Polymer-based 3D printed millimeter-wave components for spacecraft payloads," in *IEEE MTT-S Int. Microw. Symp. Dig.*, Ann Arbor, MI, USA, Jul. 2018, pp. 1–3.

[7] *TZcam Uncooled THz Imager, TZcam Datasheet*, I2S, Pessac, France, May 2019.

[8] *Microxcam-384i-THz Terahertz Camera, Microxcam-384i-THz Datasheet*, INO, New Delhi, India, 2019.

[9] *TicMOS-1kpx*. Accessed: Sep. 8, 2020. [Online]. Available: https://ticwave.com/index.php/shop/ticmos-1kpx

[10] F. Simoens, "Buyer's guide for a terahertz (THz) camera," *Photoniques Special EOS*, no. 2, pp. 58–62, Apr. 2018.

[11] F. Blanchard, J. E. Nkeck, D. Matte, R. Nechache, and D. G. Cooke, "A low-cost terahertz camera," *Appl. Sci.*, vol. 9, no. 12, pp. 1–8, Jun. 2019.

[12] *Millimeter Wave Products, Catalog*, Millitech Corp., Northampton, MA, USA, 1995.

[13] *8-bit AVR Microcontroller With 32K Bytes in-System Programmable Flash, ATmega328P Datasheet*, Atmel, San Jose, CA, USA, Jan. 2015.

[14] *8-bit Atmel Microcontroller With 16/32/64KB In-System Programmable Flash, ATmega640 datasheet*, Atmel, San Jose, CA, USA, Feb. 2014.

[15] *Ultra-Small, Low-Power, 16-Bit Analog-to-Digital Converter With Internal Reference, ADS1115 Datasheet*, Texas Instrum., Dallas, TX, USA, Oct. 2009.

[16] *Microwave Products*, Catalog Flann Microw. Ltd, Cornwall, U.K., 2007.

[17] *ϕ76.2 × 76.2mm EFL 90° OAP Protected Aluminum Mirror 100Å, 35522 Datasheet*, Edmund Optics, Barrington, NJ, USA. Accessed: Oct. 14, 2020. [Online]. Available: https://www.edmundoptics.co.uk/p/762-x-381mm-pfl-90-off-axis-parabolic-aluminum-mirror/33594/

[18] MATLAB Fspecial. (2020). *Create Predefined 2-D Filter*. Accessed: May 9, 2020. [Online]. Available: https://uk.mathworks.com/help/images/ref/fspecial.html#d120e70040
[19] A. Kazemipour, M. Hudlička, R. Dickhoff, M. Salhi, T. Keline-Ostmann, and T. Schrader, "The horn antenna as Gaussian source in the mm-wave domain," *J. Infr., Millim., Terahertz Waves*, vol. 35, no. 9, pp. 720–731, Sep. 2014.
[20] D. Gu, D. Houtz, J. Randa, and D. K. Walker, "Reflectivity study of microwave blackbody target," *IEEE Trans. Geosci. Remote Sens.*, vol. 49, no. 9, pp. 3443–3451, Sep. 2011.
[21] *MI-WAVE Millimeter Wave Products Inc. Product Catalog*. Accessed: Jul. 12, 2020. [Online]. Available: http://miwv.com/MiWave-Catalog.pdf
[22] J. Sun and S. Lucyszyn, "Extracting complex dielectric properties from reflection-transmission mode spectroscopy," *IEEE Access*, vol. 6, pp. 8302–8321, Jan. 2018.
[23] M. N. Afsar and H. Chi, "Millimeter wave complex refractive index, complex dielectric permittivity and loss tangent of extra high purity and compensated silicon," *Int. J. Infr. Millim. Waves*, vol. 15, no. 7, pp. 1181–1188, Jul. 1994.
[24] M. N. Afsar and H. Ding, "A novel open-resonator system for precise measurement of permittivity and loss-tangent," *IEEE Trans. Instrum. Meas.*, vol. 50, no. 2, pp. 402–405, Apr. 2001.
[25] *BOROFLOAT 33 High-quality Borosilicate Glass From SCHOTT*. Accessed: Jul. 10, 2020. [Online]. Available: https://www.pgo-online.com/intl/borofloat.html
[26] M. A. Towfiq, A. Khalat, B. A. Cetiner, O. Ceylan, and N. Biyikli, "Broadband high-gain 60 GHz antenna array," in *Proc. IEEE Int. Symp. Antennas Propag. (APSURSI)*, Fajardo, Puerto Rico, Jun. 2016, pp. 899–900.
[27] F. I. Shimabukuro, S. Lazar, M. R. Chernick, and H. B. Dyson, "A quasi-optical method for measuring the complex permittivity of materials," *IEEE Trans. Microw. Theory Techn.*, vol. 32, no. 7, pp. 659–665, Jul. 1984.
[28] P. Blondy, D. Cros, P. Guillon, F. Balleras, and C. Massit, "W band silicon dielectric resonator for semiconductor substrate characterization," in *IEEE MTT-S Int. Microw. Symp. Dig.*, Baltimore, MD, USA, vol. 3, Jun. 1998, pp. 1349–1352.
[29] M. N. Afsar and K. J. Button, "Precise millimeter-wave measurements of complex refractive index, complex dielectric permittivity and loss tangent of GaAs, Si, SiO_2, $A1_2O_3$, BeO, macor, and glass," *IEEE Trans. Microw. Theory Techn.*, vol. 31, no. 2, pp. 217–223, Feb. 1983.
[30] M. N. Afsar and K. J. Button, "Millimeter-wave dielectric measurement of materials," *Proc. IEEE*, vol. 73, no. 1, pp. 131–153, Jan. 1985.
[31] Y. Wang, X. Shang, N. M. Ridler, T. Huang, and W. Wu, "Characterization of dielectric materials at WR-15 band (50–75 GHz) using VNA-based technique," *IEEE Trans. Instrum. Meas.*, vol. 69, no. 7, pp. 4930–4939, Jul. 2020.
[32] D. T. F. Marple, "Refractive index on GaAs," *J. Appl. Phys.*, vol. 35, pp. 1241–1242, Nov. 1963.
[33] S. Lucyszyn, "Investigation of anomalous room temperature conduction losses in normal metals at terahertz frequencies," *IEE Proc.-Microw., Antennas Propag.*, vol. 151, no. 4, pp. 321–329, Aug. 2004.
[34] J. Sun, A. Dawood, W. J. Otter, N. M. Ridler, and S. Lucyszyn, "Microwave characterization of low-loss FDM 3-D printed ABS with dielectric-filled metal-pipe rectangular waveguide spectroscopy," *IEEE Access*, vol. 7, pp. 95455–95486, Jul. 2019.
[35] F. Costa, A. Monorchio, and G. Manara, "Analysis and design of ultra thin electromagnetic absorbers comprising resistively loaded high impedance surfaces," *IEEE Trans. Antennas Propag.*, vol. 58, no. 5, pp. 1551–1558, May 2010.

SANG-HEE SHIN (Graduate Student Member, IEEE) was born in Seoul, South Korea, in 1992. He received the M.Eng. degree in aeronautical engineering from Imperial College London, London, U.K., in 2018, where he is currently pursuing the Ph.D. degree with the Department of Electrical and Electronic Engineering.

His research interests include designing and manufacturing RF and quasi-optical systems for microwave and mm-wave applications using additive manufacturing techniques.

STEPAN LUCYSZYN (Fellow, IEEE) received the Ph.D. degree in electronic engineering from the King's College London, University of London, London, U.K., in 1992, and the D.Sc. degree (higher doctorate) in millimeter-wave and terahertz electronics from Imperial College London, London, in 2010.

From 1997 to 2012, he taught MMIC Measurement Techniques on IEE/IET short courses hosted by the U.K.'s National Physical Laboratory. He is currently a Professor of millimetre-wave systems and the Director of the Centre for Terahertz Science and Engineering, Imperial College London. He has coauthored over 200 articles and 12 book chapters in applied physics and electronic engineering. He has served as a Founding Member of the Steering Group for the U.K.'s EPSRC Terahertz Network and a member of the IEEE Technical Committee for Terahertz Technology and Applications (MTT-4). He was made a Fellow of the Institution of Electrical Engineers, U.K., and the Institute of Physics, U.K., in 2005. In 2008, he became a Fellow of the Electromagnetics Academy, USA. He was appointed as an IEEE Distinguished Microwave Lecturer from 2010 to 2013. He is also a European Microwave Lecturer of the European Microwave Association. He co-founded the Imperial College London spin-out company Drayson Wireless Ltd., in 2014.